

Indentation Pileup Behavior of Ti-6Al-4V Alloy: Experiments and Nonlocal Crystal Plasticity Finite Element Simulations



FENGBO HAN, BIN TANG, XU YAN, YIFEI PENG, HONGCHAO KOU, JINSHAN LI, YING DENG, and YONG FENG

This study reports on the indentation pileup behavior of Ti-6Al-4V alloy. Berkovich nanoindentation was performed on a specimen with equiaxed microstructure. The indented area was characterized by electron backscattered diffraction (EBSD) to obtain the indented grain orientations. Surface topographies of several indents were measured by atomic force microscopy (AFM). The pileup patterns on the indented surfaces show significant orientation dependence. Corresponding nonlocal crystal plasticity finite element (CPFE) simulations were carried out to predict the pileup patterns. Analysis of the cumulative shear strain distributions and evolutions for different slip systems around the indents found that the pileups are mainly caused by prismatic slip. The pileup patterns evolve with the loading and unloading process, and the change in pileup height due to the elastic recovery at unloading stage is significant. The density distributions of geometrically necessary dislocations (GNDs) around the indent were predicted. Simulation of nanoindentation on a tricrystal model was performed.

DOI: 10.1007/s11661-016-3946-0

© The Minerals, Metals & Materials Society and ASM International 2017

I. INTRODUCTION

NANOINDENTATION is an effective technique to evaluate the elastic modulus, hardness, and plasticity mechanisms in material science.^[1–5] Although the actual deformation process during nanoindentation is simple, the boundary conditions and kinematics involved are complex.^[6] Accordingly, the structure formation below and around indents are complex too. Material around the contact area tends to deform upwards or downwards with respect to the indented surface plane, which results in pileup or sink-in, respectively.^[2] These characteristics are due to the crystallography and the orientation of the grain indented.^[2,5,7,8] Several authors have tried to investigate the nanoindentation pileup or sink-in behavior of crystal materials, such as copper,^[2,4] aluminum,^[9] magnesium,^[7] titanium,^[5,8,10] and γ -TiAl.^[11] In most of these studies,^[2,4,7,8,10,11] an efficient method by combining application of nanoindentation, electron backscatter diffraction (EBSD) orientation mapping, atomic force microscopy (AFM) topographic measurements, and crystal plasticity finite element (CPFE) modeling was used to analyze the pileup or sink-in behavior.

As a typical $\alpha + \beta$ titanium alloy, Ti-6Al-4V has been widely used in aerospace industries, due to its low

density and attractive mechanical and corrosion-resistant properties.^[12–14] The predominant constituent phase of this alloy, low-symmetry hexagonal-structured α phase, exhibits remarkable anisotropy of elasticity and plasticity. The critical resolved shear stresses (CRSS) of different kinds of slip systems of α phase vary a lot, leading to selective activation of only a few deformation systems for many boundary conditions.^[10] Therefore, there will be a considerable heterogeneity of plastic flow during deformation at grain scale. One important deformation situation at such small scale is the aforementioned nanoindentation, during which the plastic flow of α phase is very complicated. Viswanathan *et al.*^[3,15] made direct observation and analyses of dislocation substructures in α phase of Ti-6Al-4V alloy formed by nanoindentation with TEM on the focused ion beam (FIB) cutting thin-foil membranes. Han *et al.*^[8] also studied the nanoindentation process of Ti-6Al-4V alloy by combining experiments and CPFE simulations using a local constitutive law. Although the pileup behavior of Ti-6Al-4V alloy was discussed briefly in these studies, a thorough understanding of the pileup behavior of this alloy is still lacking.

In this work, we present a detailed micromechanical analysis of indentation pileup behavior of Ti-6Al-4V alloy. To that end, a combination of nanoindentation testing, EBSD orientation mapping, AFM topographic measurements, and nonlocal CPFE simulations were performed. The experimentally observed nanoindentation pileup patterns are compared to corresponding predictions obtained by CPFE simulations. Shear strain distributions and evolutions for different slip systems around the indents were analyzed, in order to demonstrate the contributions of different slip systems for

FENGBO HAN, BIN TANG, XU YAN, YIFEI PENG, HONGCHAO KOU, JINSHAN LI, and YONG FENG are with the State Key Laboratory of Solidification Processing, Northwestern Polytechnical University, Xi'an 710072, P.R. China. Contact e-mail: toby@nwpu.edu.cn YING DENG is with the Beijing Aeronautical Manufacturing Technology Research Institute, Beijing 100024, P.R. China.

Manuscript submitted June 11, 2016.

Article published online January 17, 2017

pileup. Moreover, a tricrystal model was established and nanoindentation simulation was performed on the tricrystal junction.

II. EXPERIMENTS

The Ti-6Al-4V alloy used in the present work was heat-treated to an equiaxed microstructure, as shown in Figure 1. The sample surface was firstly ground with sand paper, then diamond-polished, and finally electro-polished with a solution of 5 pct perchloric acid in alcohol using a voltage of 30 V for 240 seconds at 298 K (25 °C). A good surface quality satisfying the requirements for nanoindentation test and EBSD examination can be obtained through this way. Nanoindentation tests were conducted in an Agilent G200 tester equipped with a Berkovich diamond indenter at room

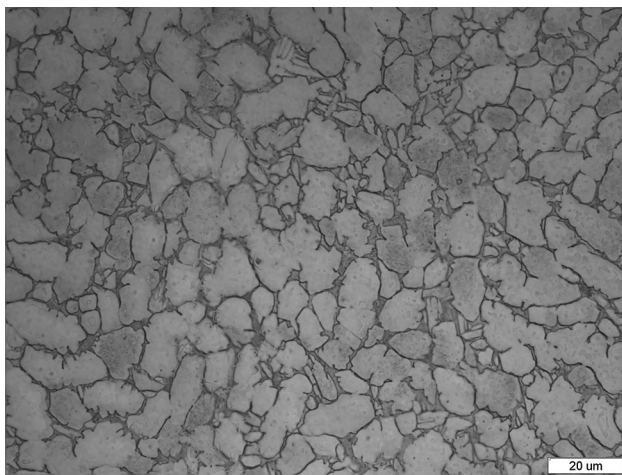


Fig. 1—Microstructure of the Ti-6Al-4V alloy.

temperature under the laboratory environment. The maximum indentation depth is 200 nm, loading for 5 seconds at constant rate (*i.e.*, the loading rate is 40 nm/s), then holding for 2 seconds at the depth limit, and then unloading for 5 seconds at constant rate. After an array of nanoindents was made, the sample was analyzed in a ZEISS SUPRA55 SEM operating at 20 kV

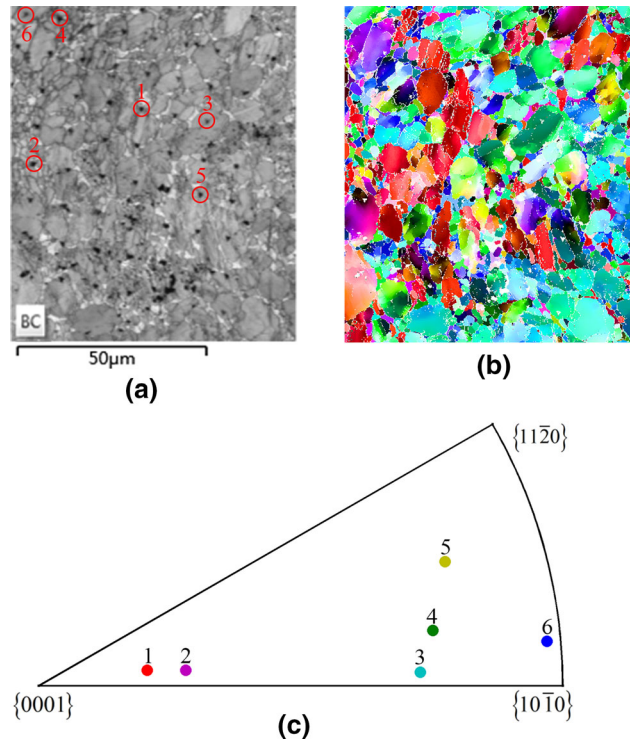


Fig. 3—An array of indents applied on the Ti-6Al-4V sample surface. (a) Kikuchi band contrast map (b) EBSD orientation maps (c) Inverse pole figure showing the orientations of the six marked grains with nanoindents.

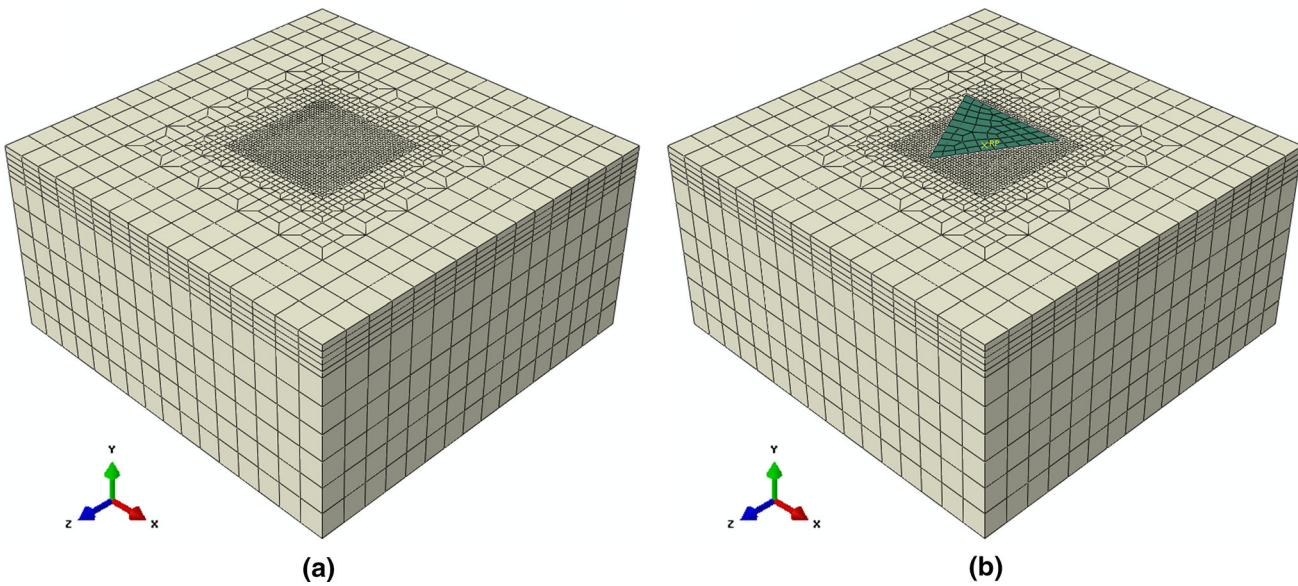


Fig. 2—Finite element model of nanoindentation. (a) without indenter grid (b) with indenter grid.

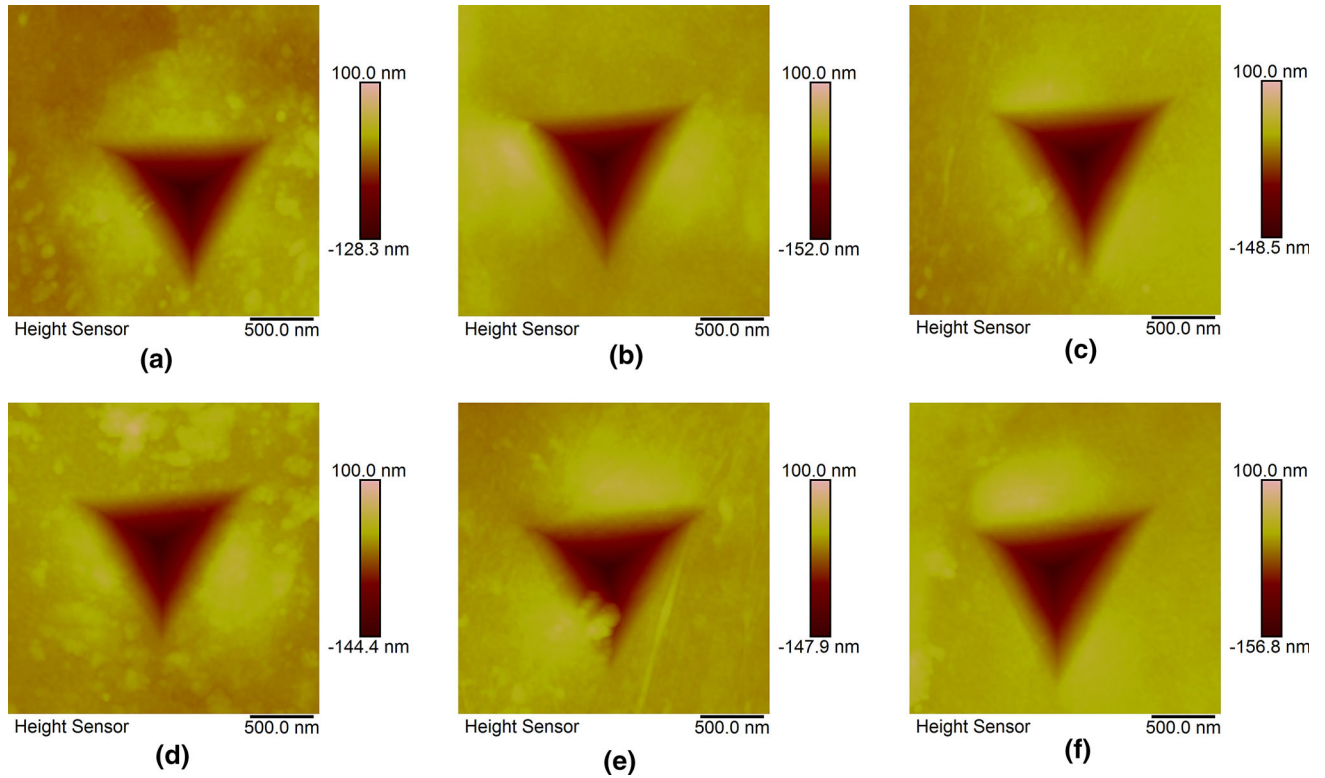


Fig. 4—AFM images of the pileup patterns for the six indents, where (a) through (f) corresponding to the numbered (1 to 6) grain orientations in Fig. 3(c).

Table I. Ti-6Al-4V Crystal Plasticity Model Parameters

Slip Systems	$\dot{\gamma}_0$	n	k_0	h_0 (MPa)	g_0 (MPa)	g_s (MPa)
Basal $\langle a \rangle$	0.001	15	2	600	420	462
Prismatic $\langle a \rangle$				410	370	407
Pyramidal $\langle a \rangle$				410	490	539

Table II. Elastic Constants of α Phase for Ti-6Al-4V Alloy^[22]

C_{11}	C_{12}	C_{13}	C_{33}	C_{44}
162,400 MPa	92,000 MPa	69,000 MPa	180,700 MPa	49,700 MPa

and equipped with a Nordlys EBSD detector and the TSLOIM EBSD software. The surface topography around nanoindent was measured by Bruker Dimension® Icon™ AFM.

III. CRYSTAL PLASTICITY FINITE ELEMENT METHOD

A. Nonlocal Crystal Plasticity Constitutive Model

The CPFEM frame and method based on the works of Asaro and Needleman^[16] and Peirce *et al.*^[17] is employed. Generally, the plastic deformation follows Schmid's law. Once the resolved shear stress in a slip system approaches a certain critical value, the slip

system will be active, and plastic deformation begins. Hutchinson^[18] proposed a simple rate-dependent power law relation to determine the shear strain rate $\dot{\gamma}^\alpha$ of the α th slip system:

$$\dot{\gamma}^\alpha = \dot{\gamma}_0^\alpha \left| \frac{\tau^\alpha}{g^\alpha} \right|^n \text{sgn}(\tau^\alpha), \quad [1]$$

where $\dot{\gamma}_0^\alpha$ is the reference strain rate, τ^α is the resolved shear stress, g^α is the slip system strength or resistance to shear, and n is the inverse strain rate sensitivity exponent. The evolution of slip system deformation resistance is controlled by two types of dislocations, *viz.* statistically stored dislocations (SSDs) and geometrically necessary dislocations (GNDs). Strain hardening arising from the accumulation of dislocations is

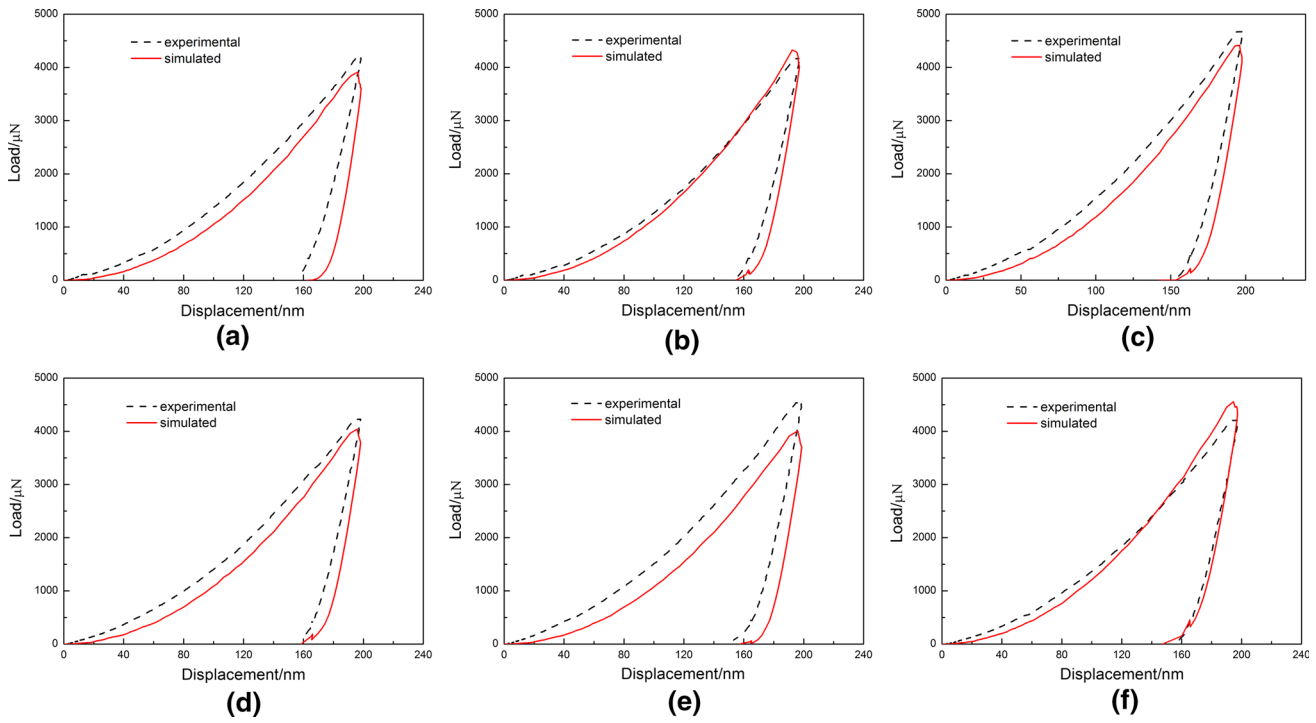


Fig. 5—Load–displacement curves for the six grain orientations, where (a) through (f) corresponding to the numbered (1 to 6) grain orientations in Fig. 3(c).

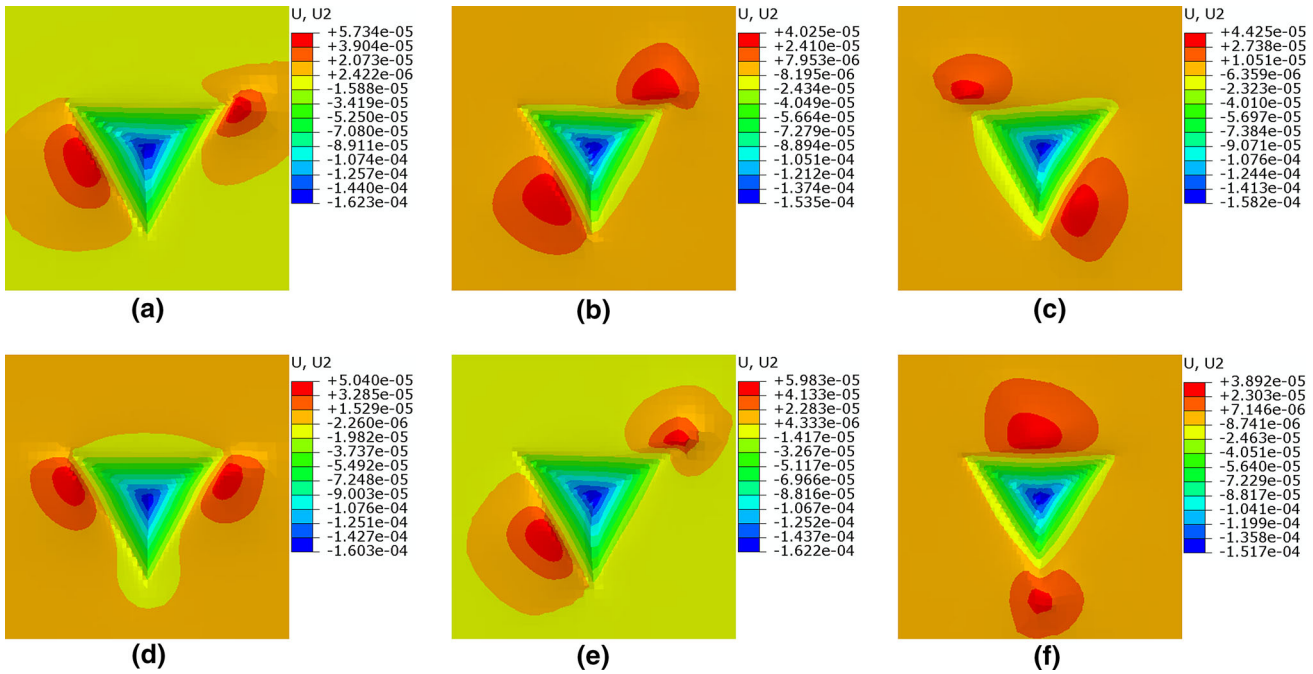


Fig. 6—Simulated pileup patterns for the six indents, where (a) through (f) corresponding to the numbered (1 to 6) grain orientations in Fig. 3(c).

characterized by the evolution of the rate of change of yield strengths:

$$\dot{g}^{\alpha} = \sum_{\beta} h_{\alpha\beta} \dot{\gamma}^{\beta} + \frac{k_0 \dot{\alpha}^2 G^2 b}{2(g^{\alpha} - g_0^{\alpha})} \sum_{\beta} \lambda^{\beta} \dot{\gamma}^{\beta}. \quad [2]$$

The first item in Eq. [2] corresponds to strain hardening caused by SSDs. $h_{\alpha\beta}$ are the matrix of slip hardening moduli. The hardening model of Asaro and Needleman,^[16] and Pierce *et al.*^[17] is adopted here, in which the self-hardening moduli is expressed as follows:

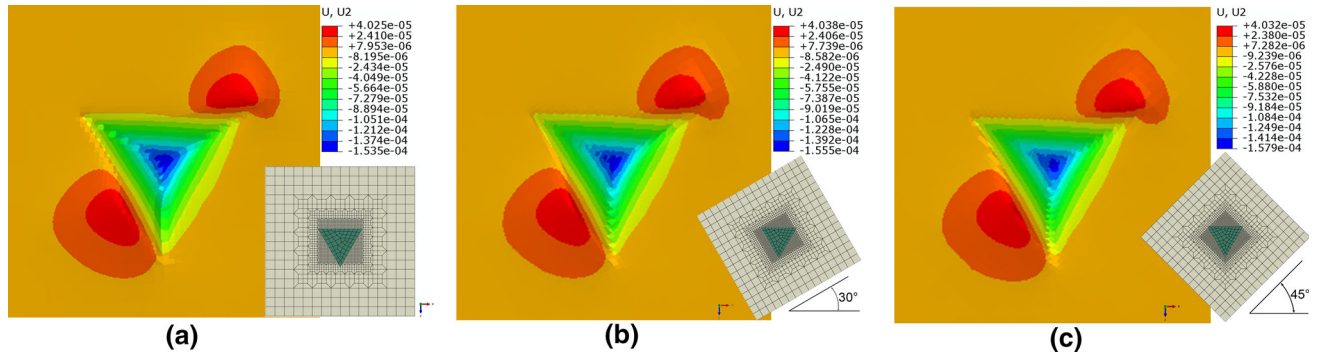


Fig. 7—Simulated pileup patterns for different grid orientations. (a) not rotated (b) rotated 30 deg (c) rotated 45 deg.

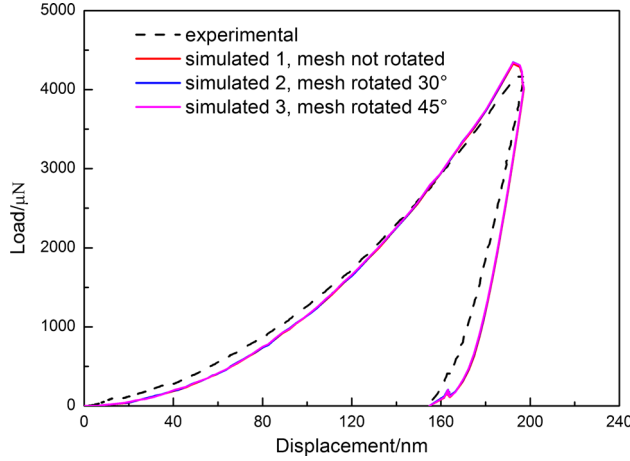


Fig. 8—Load-displacement curves for different grid orientations.

$$h_{\alpha\alpha} = h(\gamma) = h_0 \sec h^2 \left| \frac{h_0 \gamma}{g_s - g_0} \right|, \quad [3]$$

where h_0 is the initial hardening modulus, g_0 is the initial value of the slip resistance (*i.e.*, critical resolved shear stress, CRSS), g_s is the saturation value, and γ is the Taylor cumulative shear strain on the all activated slip systems.

The latent hardening moduli are given by

$$h_{\alpha\beta} = qh(\gamma) \quad (\alpha \neq \beta), \quad [4]$$

where q is the latent hardening parameter.

The second term in Eq. [2] accounts for the effect of GNDs on work hardening developed by Acharya and Beaudoin.^[19] In this item, k_0 is a dimensionless material constant, b is the Burgers vector, G is the elastic shear modulus, and $\hat{\alpha}$ is a nondimensional constant. $\hat{\alpha}$ is taken to be 1/3 in Reference 20 λ^β is a measure of linear dislocation density along a slip plane, and is given by

$$\lambda^\beta = \sqrt{\Lambda n^\beta : \Lambda n^\beta}, \quad [5]$$

where \mathbf{n}^β is a slip plane normal and Λ is an incompatibility tensor. Λ can be expressed using the curl of plastic deformation gradient tensor \mathbf{F}^P . Specifically,

$$\Lambda = \nabla \times \mathbf{F}^P \quad [6]$$

B. Finite Element Implementation

The crystal plasticity constitutive model was implemented to user material subroutine (UMAT) of the implicit finite element code ABAQUS/Standard. Stress state and the solution-dependent state variables during deformation are updated through the subroutine, which also provides the material Jacobian matrix needed by ABAQUS/Standard. A 3D model for nanoindentation was created. Figure 2(a) shows only the grid of the specimen, and Figure 2(b) shows the assembled meshes with Berkovich indenter on the surface of the specimen. The Berkovich indenter was set as a discrete rigid, while the specimen was set as deformable part consisting of 14,520 eight-node linear solid elements and 16,236 nodes (C3D8). A transition mesh technique was used and meshes at the contact area are much finer (the minimum element size is 40 nm) than other regions, which was expected to provide a better FEM simulation accuracy, and the size of mesh was optimized to avoid excessive element distortion. The dimensions of the specimen are $5.12 \times 2.56 \times 5.12 \mu\text{m}^3$ ($X \times Y \times Z$). The thickness of the specimen is large enough to avoid the influence from the substrate, since the maximum depth of indentation is no more than 200 nm. The bottom surface and four surrounding surfaces of the specimen model were constrained along three axes by considering the real conditions of indentation (the sample for indentation was stuck on the platform with the top surface free). The contact surface is assumed to be frictionless. Consistent with the experimental loading mode, the displacement of the Berkovich indenter was controlled during nanoindentation simulations, and the maximum displacement is 200 nm, loading for 5 seconds at constant rate (*i.e.*, the displacement rate is 40 nm/s), then holding for 2 seconds at the maximum displacement, and then unloading for 5 seconds at constant rate.

IV. RESULTS AND DISCUSSION

An array of indents was applied on the Ti-6Al-4V sample surface. Figure 3(a) shows the Kikuchi band contrast map of the indented area, from which the

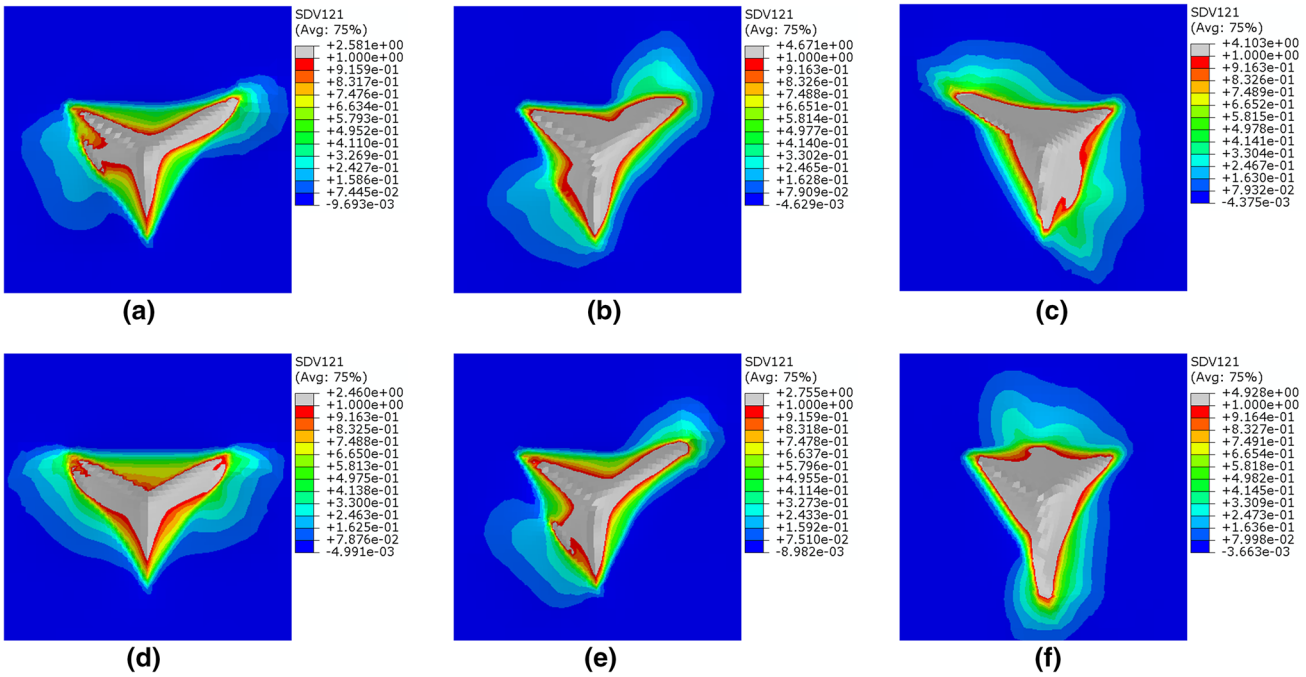


Fig. 9—Simulated shear strain distributions for the six indents, where (a) through (f) corresponding to the numbered (1 to 6) grain orientations in Fig. 3(c). Large strains beneath the indenter are set to gray, in order to distinguish the strains concentration at the locations of pileups more clearly.

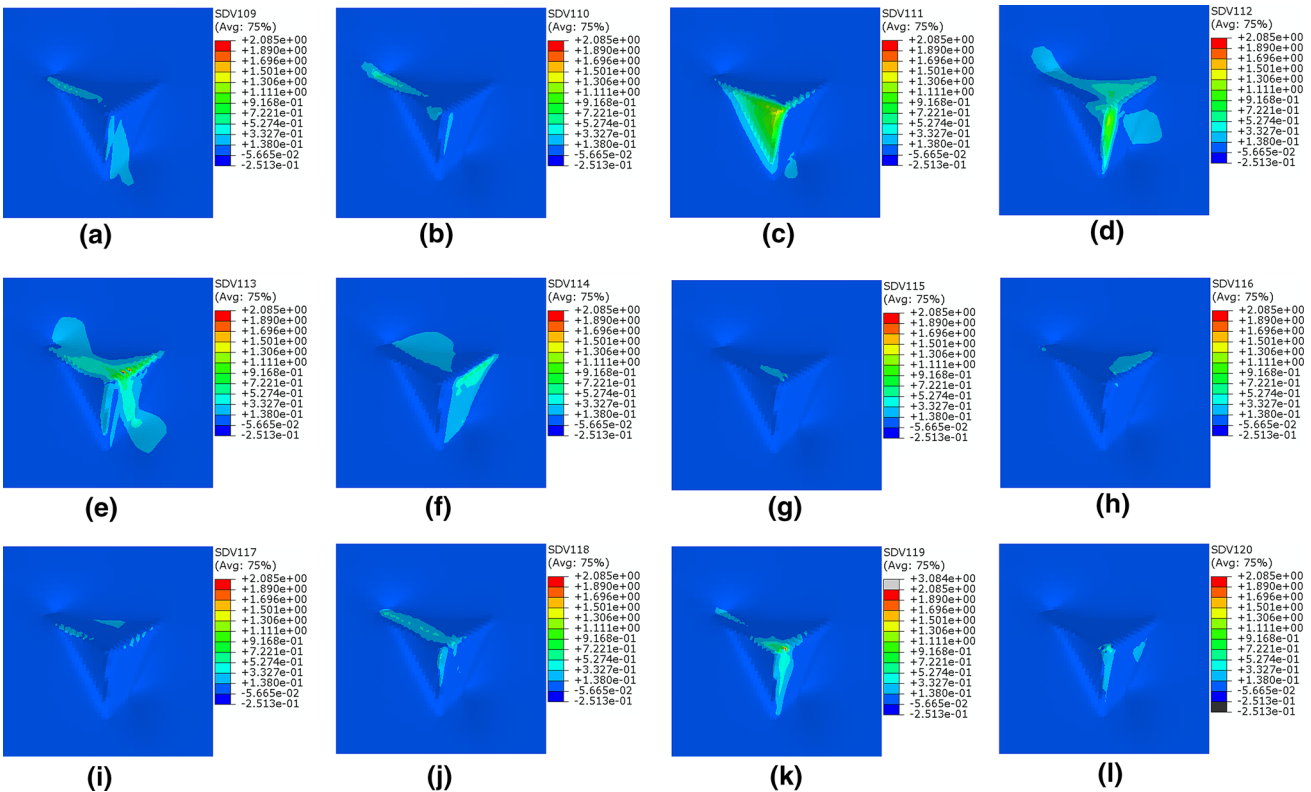


Fig. 10—Simulated shear strain distributions on 12 slip systems after nanoindentation for indent numbered 3 (a) (0001)[1120] (b) (0001)[1210] (c) (0001)[2110] (d) (1100)[1120] (e) (1010)[1210] (f) (0110)[2110] (g) (1101)[1120] (h) (1010)[1210] (i) (0111)[2110] (j) (1101)[1120] (k) (1011)[1210] (l) (0111)[2110], where (a) through (c) are basal slip systems, (d) through (f) are prismatic slip systems, and (g) through (l) are pyramidal $\langle a \rangle$ slip systems.

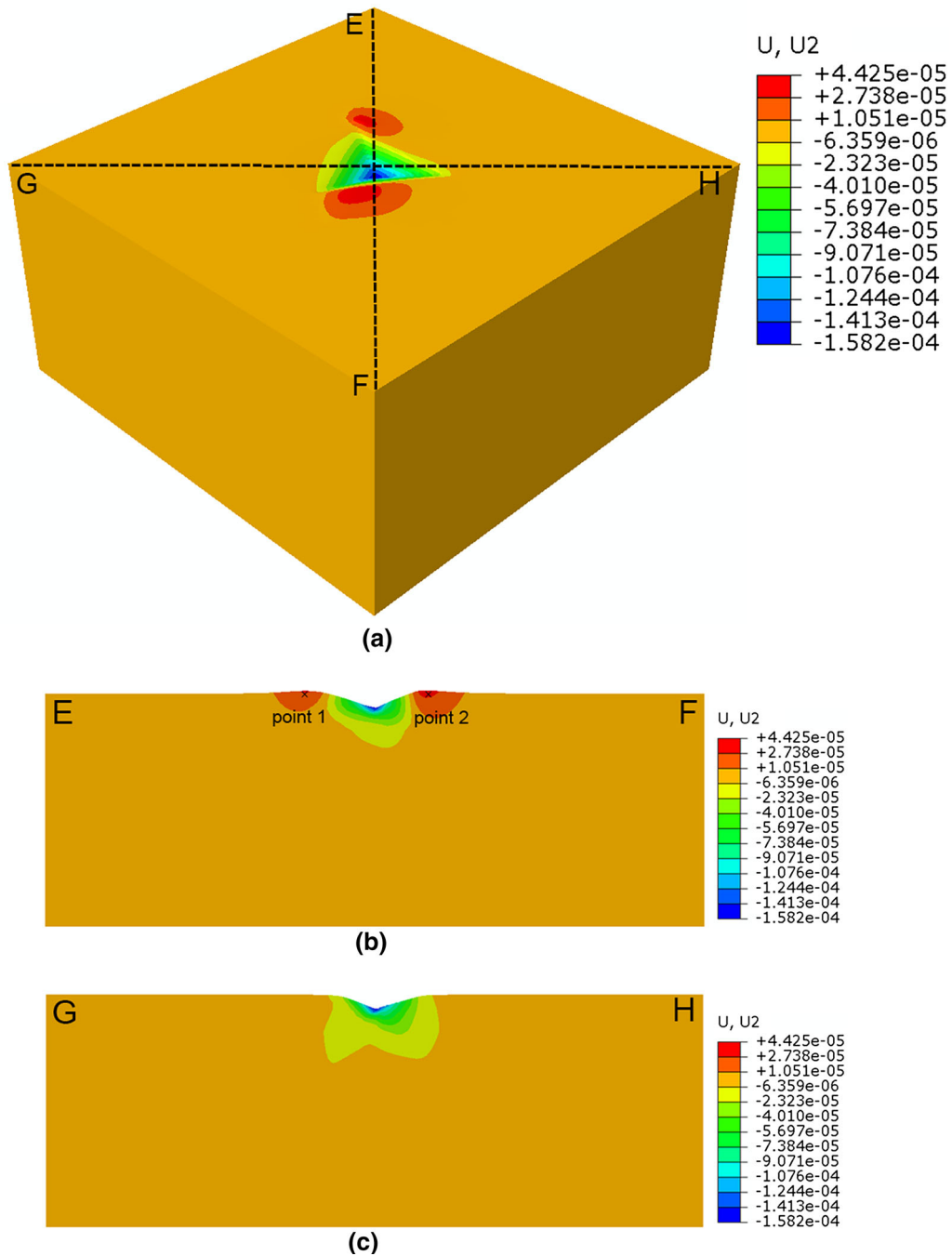


Fig. 11—Simulated pileup pattern for indent numbered 3 (a) 3D view (b) section *EF* (c) section *GH*. It should be noted that (b) and (c) used the same colorbar in (a).

indents can be identified, and Figure 3(b) shows the corresponding EBSD orientation maps generated by an open source software toolbox named MTEX.^[21] Comparing Figures 3(a) and (b), orientations of all the grains with indents can be determined. Six selected indents in Figure 3(a) are marked by red circles and numbers, and the orientations of which are shown in the inverse pole figure (IPF) of Figure 3(c). The AFM images of the pileup patterns for the six different indents are shown in Figure 4. Clearly, we can see that

there are obvious pileups around the indents. The locations of pileups for different indents vary from each other. It indicates orientation-dependent nature of the pileup behavior. For each indent, there are usually two hillocks locating at two opposite sides of the Berkovich indenter, and one is usually higher and larger than the other. This reflects the localized plastic flow character of single crystal, which essentially relates to the crystallographic slip systems of hexagonal structure.

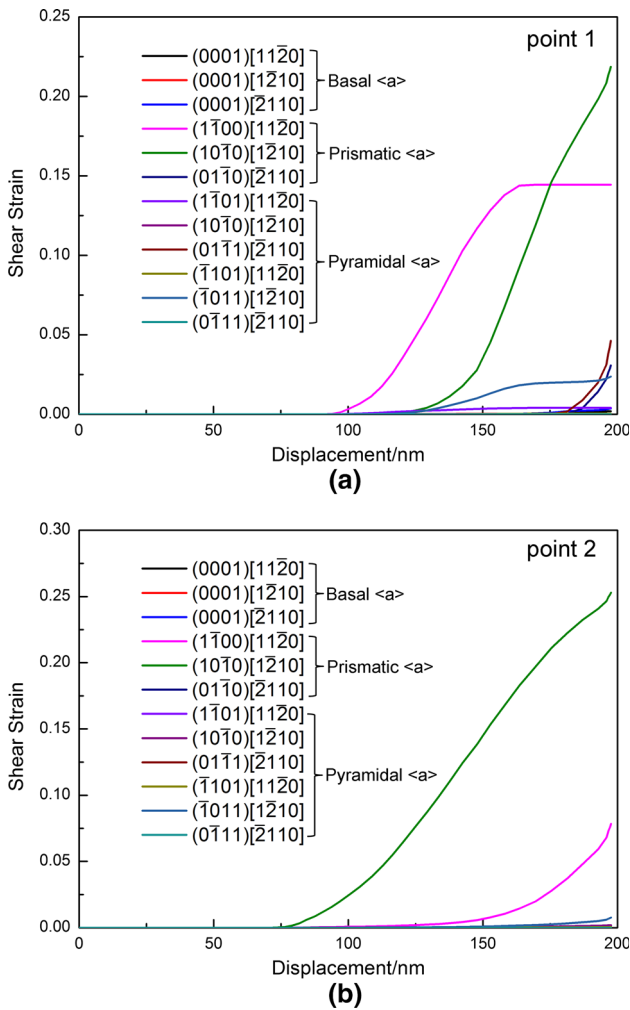


Fig. 12—Evolution of shear strain on different slip systems at two points (a) point 1 (b) point 2 in Fig. 9(b). The two points are located at the nodes with local maximum displacements at the two pileup regions in the section after indentation, respectively.

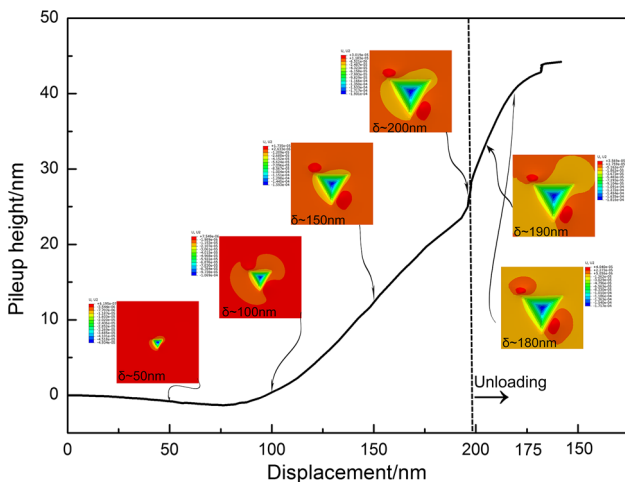


Fig. 13—Evolution of height of the top of the pileup for indent numbered 3. The insets in this figure show the pileup patterns at different indenter displacements (δ) during loading and unloading process.

Nonlocal CPFЕ nanoindentation simulations were performed with the six grain orientations as shown in Figure 3(c). The basal, prismatic, and pyramidal $\langle a \rangle$ families of slip systems commonly activated in α phase are considered. The material parameters for these slip systems are obtained by fitting the simulated load–displacement curves with the experimental curves. The reported parameters of alpha phase for Ti-6Al-4V in the literature^[22] were referenced, and adjustment was made through trial-and-error method to reduce the error between the simulated and experimental load–displacement curves. The fitted parameters are listed in Table I. The reference strain rate $\dot{\gamma}_0^z$ and inverse strain rate sensitivity exponent n are kept the same with that in the literature,^[22] and fitting is mainly made on parameters h_0 , g_0 , g_s , and k_0 . The CRSS of prismatic, basal, and pyramidal slip systems are 370, 420, and 490 MPa, respectively, which are reasonable in their magnitudes and hierarchy, as commonly believed that the prismatic slip systems have the lowest CRSS and the pyramidal slip systems have the largest CRSS for titanium alloy. The elastic constants of α phase are listed in Table II, which are also obtained from Reference 22. Figure 5 shows the experimental and simulated load–displacement curves of nanoindentation for the six grain orientations. For orientations numbered 2 and 6, the simulated curves are very close to the experimental curves, while the simulated curves for others are slightly deviated from the experimental curves. The deviations between the experimental and simulated curves are mainly from the experimental error and the error arises by crystal plasticity constitutive model parameters. As the rate-dependent power law crystal plasticity constitutive model was used in the CPFЕ simulations, the stress relaxation effect during holding process was captured in simulations, and the load tends to decrease at the holding process, resulting convex profile at the top of the load–displacement curve. While the relaxation phenomena in nanoindentation experiment are not obvious, there is no obvious convex profile at the top of the load–displacement curve. Overall, the simulated error is acceptable, and the CPFЕ model and the determined material parameters are appropriate.

Figure 6 shows the simulated pileup patterns for the six indents. It should be noted that the pileup patterns are considered to be the displacement distributions along the reverse of indentation direction, *i.e.*, U2. The regions with large positive displacement along indentation direction are considered to be pileup regions. Apparently, there are two pileups locating at two opposite sides of the Berkovich indenter. In comparison with the AFM images of the pileup patterns in Figure 4, the locations of the simulated pileups are roughly consistent with the experimental ones. Figures 6(c), (d), and (f) are much similar to the experimental results, while others show relatively larger differences. Since the pileup patterns obtained from AFM tests are significantly affected by the surface quality of the samples, the degradation of the sample surface quality during the process of experiments is the main source of the error.

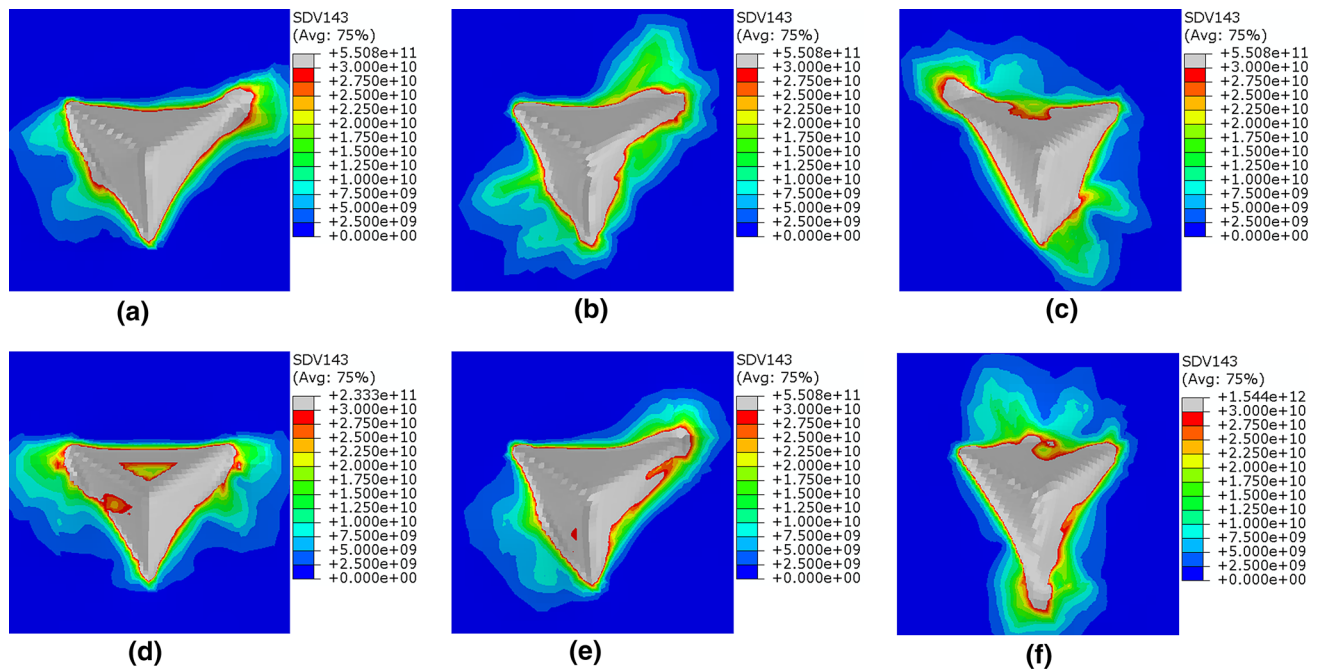


Fig. 14—Simulated GND density distributions for the six indents, where (a) through (f) corresponding to the numbered (1 to 6) grain orientations in Fig. 3(c). Large GND densities beneath the indenter are set to gray, in order to distinguish the GND densities concentration at the locations of pileups more clearly.

As a “square” FEM grid was used to model indentation with a pyramidal indenter in this study, and the finest meshed zone is also a square region, the orientation of the grid relative to the indenter may affect the simulation results. In order to investigate this issue, another two nanoindentation FEM models were created, in which the meshes are rotated 30 and 45 deg relative to the indenter, respectively. Figure 7 shows the simulated pileup patterns for the three grid orientations. The grain orientations in the three models are set the same (orientation numbered 2 in Figure 3(c)). It can be seen that differences of pileup patterns between different grid orientations are very small, which can be neglected. Figure 8 depicts the load–displacement curves for different grid orientations, and the curves for three grid orientations almost entirely coincided with each other. This also indicates that the effect of grid orientation relative to the indenter on the simulation result is very small.

Figure 9 illustrates the simulated shear strain distributions for the six indents. Shear strains where the pileups located are relatively larger than that at adjacent place with no pileups. It is easy to understand that the pileups result from the anisotropic plastic shear deformation. As the shear strains shown in Figure 9 are total strains arising from all the activated slip systems, it is unable to state clearly which slip systems are predominant for the pileups from this figure. In order to distinguish the contributions of different slip systems on the pileups, the indent numbered 3 is selected and the simulated shear strain distributions on 12 slip systems are shown in Figure 10. From Figures 10(d) and (e), we can find that shear strains on the two slip systems, (1-100)[11–20] and (10-10)[1-210], which are prismatic

slip systems, concentrate at where the pileups located. So, it can be concluded that the pileups are mainly caused by prismatic slip.

Figure 11(a) shows the simulated pileup pattern for indent numbered 3 in 3D view. Figures 11(b) and (c) show the two sections vertically cutting along the dash lines *EF* and *GH* in Figure 11(a). The two lines are the diagonals of the upper surface of the cube model, and one through the two pileups and the other not, so the situations of pileup regions and no pileup regions beneath the surface can be compared by observing the two sections. In another word, the interior of pileup can be observed from the section view. The regions of two pileups can be identified clearly from the section view in Figure 11(b), for where there is a larger positive displacement along the reverse of indentation direction than other regions. This implies that materials at some local regions around the indenter tend to flow upwards during indentation. In the section shown in Figure 11(c), all the materials flow downwards, showing significant difference from that in Figure 11(b). This also reflects the anisotropic nature of plastic flow in single crystal.

Two points at the pileup regions are marked in Figure 11(b), and they are located at the nodes with local maximum displacements at the two pileup regions in the section after indentation, respectively. The evolutions of shear strain on different slip systems at these two points during loading stage of nanoindentation are illustrated in Figure 12. At both locations, incipient plasticity occurs after some indentation displacements ($\delta \sim 75$ nm). Prismatic $\langle a \rangle$ slip systems are the firstly activated at the two locations. The total accumulated strains on prismatic $\langle a \rangle$ slip systems are maximum at the end of the loading stage, and those on basal and

pyramidal are negligibly small. This indicates the prismatic $\langle a \rangle$ slip systems contribute the most to the pileup compared to other slip systems. Considering that the CRSS of prismatic $\langle a \rangle$ slip system is the lowest, this also is an important reason as the pileups are mainly caused by prismatic $\langle a \rangle$ slip, since the prismatic $\langle a \rangle$ slip systems are more easy to activate due to their low CRSS.

Figure 13 shows the evolution of height of the top of the pileup for indent numbered 3 in the loading and unloading stages. The top of the pileup refers to the position of node that has global maximum displacement after indentation. At early stage of indentation ($\delta < 75$ nm), the height decreases with increase of indenter displacement, because the location is purely subjected to elastic deformation. Afterward, plastic deformation begins and the height increases gradually due to localized material accumulation. At unloading stage, during which elastic recovery occurs, there is a relatively large springback amount (~ 20 nm, which is nearly one half of the pileup height). Although “springback” is used here, it does not mean the pileup height will decrease at unloading stage. On the contrary, the pileup height will increase as matrix materials beneath indenter rebound at unloading stage actually. The evolution of pileup height during unloading stage is not linear, due to the complicated boundary conditions of nanoindentation with Berkovich indenter.

The insets in Figure 13 show the pileup patterns at different indenter displacements during loading and unloading process. As the indenter displacement increases, the indentation impression becomes bigger and the pileup pattern evolves. Two hillocks appear when the indenter displacement exceeds 100 nm. The pileups after completely unloaded are more distinct than that before unloading, which also indicates that the change in pileup height due to the elastic recovery is significant.

Figure 14 shows the simulated GND density distributions for the 6 indents. There is no doubt that the plastic flow beneath the indenter is very heterogeneous, resulting in large strain gradient and GND density. Here, we focus on the GND density distributions around the indenter, especially the locations of pileups. GND densities at where the pileups located are relatively larger than that at adjacent place with no pileups. This implies that the plastic strain gradient is relatively large at the pileup region.

In the present work, all the simulations of nanoindentation on single crystal of α phase in Ti-6Al-4V alloy show two hillocks. Although we used the Berkovich indenter, other than an axisymmetric conical indenter, it has little effect on the position of pileup developed for a specific orientation, and this has been proved in Reference 8. Some other works also reported the number of indentation hillocks for different alloys. Zambaldi *et al.*^[10] simulated the pileup topographies of commercial purity titanium for a number of orientations with conical indenter, and their results indicated that indented grains with orientations away from the c -axis showed two dominant hillocks on opposite sides of the indent. In another work of Zambaldi *et al.*,^[11] the

number of dominant hillocks of the face-centered cubic (fcc)-derived tetragonal structure γ -TiAl after axisymmetric indentation ranges from one, for an [111] indentation axis, to four, for axes [001] and [100]. So, the number of hillocks depends on crystal structure and the symmetry of indentation axes. For high symmetry crystal structure and indentation axes, there will be more hillocks.

As aforementioned, usually nanoindentation on single crystal of α -titanium shows two hillocks. In Reference 8, nanoindentation on bicrystal also shows two hillocks. In this work, we established a tricrystal model, as shown in Figure 15(a), in order to study the pileup behavior of tricrystal. Three grain orientations, numbered 1, 3, and 6 in IPF, as shown in Figure 3(c), are assigned to the tricrystal model. The three orientations (pileup patterns for which have relatively large distinctions, as shown in Figure 6) are selected purposely, since we expect to obtain a pileup pattern with three hillocks. The simulated pileup pattern of nanoindentation on tricrystal junction is shown in Figure 15(b). As expected, there are three hillocks located by the three edge of the Berkovich indenter. This indicates that the pileup behavior is

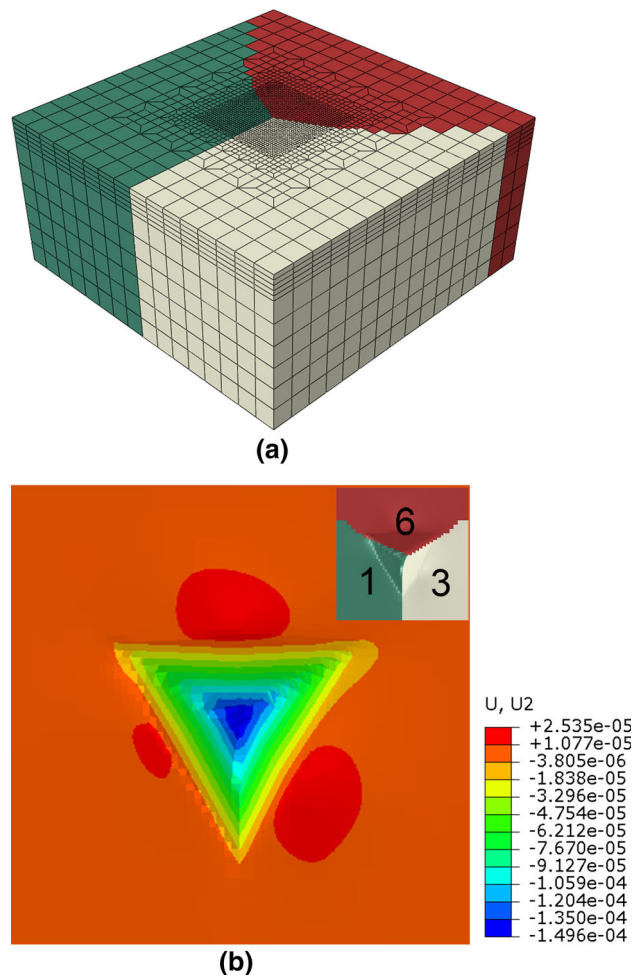


Fig. 15—(a) Tricrystal model for nanoindentation simulation (b) Simulated pileup pattern of nanoindentation on tricrystal junction. Numbers 1, 3, and 6 in the inset correspond to grain orientations in IPF of Fig. 3(c).

essentially orientation-dependent, even in very complicated boundaries conditions. The three hillocks exhibit some difference (one small, and the other two large), where orientation 1 (indentation direction is near [0001] axis) is harder than orientations 3 and 6.

V. CONCLUSIONS

In this work, we investigated the indentation pileup behavior of Ti-6Al-4V alloy by combining experiments and nonlocal CPFPE simulations. Both AFM tests and simulations show that the pileup patterns on the indented surfaces exhibit significant orientation dependence. Shear strain distributions on different slip systems around the indents reveal that the pileups are mainly caused by prismatic slip. The evolutions of shear strain on different slip systems at where the pileup appears also show that prismatic slip is the predominant deformation mechanism during nanoindentation. The pileup patterns evolve with the loading and unloading process, and the change in pileup height due to the elastic recovery at unloading stage is significant. GND densities at the pileup regions are relatively larger than that at adjacent place with no pileups. The number of hillocks depends on the crystal structure and the symmetry of indentation axes. Usually, there are two hillocks for single crystals of α -titanium with orientations away from the c -axis. A pileup pattern with three hillocks was obtained by simulation of nanoindentation on a tricrystal model.

ACKNOWLEDGMENTS

This work was financially supported by the Natural Science Foundation of Shaanxi Province (2014JQ6216), the Fundamental Research Funds for the Central Universities in China (3102015BJ(II)JGZ005), the “111” Project (No.

B08040), and the “Gao Feng” project for undergraduate.

REFERENCES

1. A.A. Elmustafa and D.S. Stone: *J. Mech. Phys. Solids*, 2003, vol. 51, pp. 357–81.
2. Y. Wang, D. Raabe, C. Klüber, and F. Roters: *Acta Mater.*, 2004, vol. 52, pp. 2229–38.
3. G.B. Viswanathan, E. Lee, D.M. Maher, S. Banerjee, and H.L. Fraser: *Acta Mater.*, 2005, vol. 53, pp. 5101–15.
4. N. Zaafarani, D. Raabe, R.N. Singh, F. Roters, and S. Zaefferer: *Acta Mater.*, 2006, vol. 54, pp. 1863–76.
5. A.F. Gerday, M. Ben Bettaieb, L. Duchêne, N. Clément, H. Diarra, and A.M. Habraken: *Acta Mater.*, 2009, vol. 57, pp. 5186–95.
6. C. Reuber, P. Eisenlohr, F. Roters, and D. Raabe: *Acta Mater.*, 2014, vol. 71, pp. 333–48.
7. B. Selvarajou, J.H. Shin, T.K. Ha, I. Choi, S.P. Joshi, and H.N. Han: *Acta Mater.*, 2014, vol. 81, pp. 358–76.
8. F.B. Han, B. Tang, H.C. Kou, J.S. Li, and Y. Feng: *Mater. Sci. Eng. A*, 2015, vol. 625, pp. 28–35.
9. M. Liu, A.K. Tieu, C. Lu, H.T. Zhu, and G.Y. Deng: *Comput. Mater. Sci.*, 2014, vol. 81, pp. 30–38.
10. C. Zambaldia, Y.Y. Yang, T.R. Bieler, and D. Raabe: *J. Mater. Res.*, 2012, vol. 27, p. 357.
11. C. Zambaldi and D. Raabe: *Acta Mater.*, 2010, vol. 58, pp. 3516–30.
12. T. Seshacharyulu, S.C. Medeiros, W.G. Frazier, and Y. Prasad: *Mater. Sci. Eng. A*, 2000, vol. 284, pp. 184–94.
13. M. Vanderhastan, L. Rabet, and B. Verlinden: *Mater. Des.*, 2008, vol. 29, pp. 1090–98.
14. T.I. Wu and J.C. Wu: *J. Alloys Compd.*, 2008, vol. 466, pp. 153–59.
15. G.B. Viswanathan, E. Lee, D.M. Maher, S. Banerjee, and H.L. Fraser: *Mater. Sci. Eng. A*, 2005, vols. 400–401, pp. 463–66.
16. R.J. Asaro and A. Needleman: *Acta Metall.*, 1985, vol. 33, pp. 923–53.
17. D. Peirce, R.J. Asaro, and A. Needleman: *Acta Metall.*, 1983, vol. 31, pp. 1951–76.
18. J.W. Hutchinson: *Proc. R. Soc. Lond. A*, 1976, vol. 348, pp. 101–27.
19. A. Acharya and A.J. Beaudoin: *J. Mech. Phys. Solids*, 2000, vol. 48, pp. 2213–30.
20. M. Anahid, M.K. Samal, and S. Ghosh: *J. Mech. Phys. Solids*, 2011, vol. 59, pp. 2157–76.
21. F. Bachmann, R. Hielscher, and H. Schaeben: *Solid State Phenomena*, 2010, vol. 160, pp. 63–68.
22. F. Bridier, D.L. McDowell, P. Villechaise, and J. Mendez: *Int. J. Plast.*, 2009, vol. 25, pp. 1066–82.